Atmos. Meas. Tech. Discuss., 7, 9095–9135, 2014
www.atmos-meas-tech-discuss.net/7/9095/2014/
doi:10.5194/amtd-7-9095-2014

Atmospheric Measurement Techniques Discussions
Open Access

Global scale remote sensing of water isotopologues in the troposphere: representation of first-order isotope effects

S. J. Sutanto[1,2], G. Hoffmann[1,3], R. A. Scheepmaker[4], J. Worden[5], S. Houweling[1,4], K. Yoshimura[6], I. Aben[4], and T. Röckmann[1]

[1]Institute for Marine and Atmosphere Research Utrecht, University of Utrecht, Princetonplein 5, 3584CC, Utrecht, the Netherlands
[2]Research Center for Water Resources, Ministry of Public Works, Jl. Ir. H. Djuanda 93, Bandung 40135, Indonesia
[3]Laboratorie des Sciences du Climat et de l'Environnement, LSCE-Orme, point courrier 129, CEA-Orme des Merisiers, 91 GIF-SUR-YVETTE CEDEX, France
[4]SRON Netherlands Institute for Space Research, Sorbonnelaan 2, 3584CA, Utrecht, the Netherlands
[5]Jet Propulsion Laboratory/California Institute of Technology, Pasadena, California, USA
[6]Atmosphere and Ocean Research Institute, University of Tokyo, Kashiwa, Japan

Received: 16 May 2014 – Accepted: 13 August 2014 – Published: 9 September 2014

Correspondence to: S. J. Sutanto (s.j.sutanto@uu.nl)

Published by Copernicus Publications on behalf of the European Geosciences Union.

AMTD
7, 9095–9135, 2014

Abstract

Over the last-decade, global scale datasets of atmospheric water vapor isotopologues (HDO) have become available from different remote-sensing instruments. Due to the observational geometry and the spectral ranges that are used, only few satellites sample water isotopologues in the lower troposphere, where the bulk of hydrological processes within the atmosphere take place. Here, we compare three satellite HDO datasets, two from the Tropospheric Emission Spectrometer (TES retrieval version 4 and 5) and one from SCIAMACHY (SCanning Imaging Absorption spectroMeter for Atmospheric CHartographY), with results from the atmospheric global circulation model ECHAM4 (European Center HAMburg 4). We examine a list of known isotopologue effects to qualitatively benchmark the various observational datasets. TES version 5 (TES_{V5}), TES version 4 (TES_{V4}), SCIAMACHY, ECHAM, and ECHAM convoluted with averaging kernel of TES version 5 ($ECHAM_{AK5}$) successfully reproduced a number of established isotopologue effects such as the latitude effect, the amount effect, and the continental effect, but to different extent. The improvement of TES version 5 over version 4 was confirmed by the steeper latitudinal gradient at higher latitudes in agreement with SCIAMACHY. Other features of the water isotopologue cycle such as the seasonally varying signal in the tropics due to the movement of the Inter Tropical Convergence Zone (ICTZ) are captured in TES_{V5} and SCIAMACHY. We suggest that the qualitative and quantitative tests carried out in this study could become benchmark tests for evaluation of future satellite isotopologue datasets.

1 Introduction

Heavy isotopologues of atmospheric water (principally HDO and $H_2{}^{18}O$) are important tracers that are widely used to derive information on moisture recycling, cloud physics, troposphere–stratosphere exchange, climate change, and paleoclimate (Jouzel et al., 1997; Worden et al., 2006; Herbin et al., 2007; Uemura et al., 2008; Frankenberg et al.,

AMTD
7, 9095–9135, 2014

2009; Field, 2010; Steinwagner et al., 2010). Equilibrium and kinetic isotope effects in the hydrological cycle, associated mainly with evaporation, condensation, and diffusion can be measured (and modeled) with high precision.

Due to the high potential of these measurements, the Global Network of Isotopes in Precipitation (GNIP) has been operational for several decades (Aggarwal et al., 2007). Compared to this global scale international activity directed at precipitation, only very few measurements were directed at measuring water vapor, because of the logistical effort required for sampling water vapor using mechanical cold trap devices (e.g. Ehhalt et al., 1989; Franz and Röckmann, 2005). Nevertheless, the bulk of water in the atmosphere is in the vapor phase and the liquid fraction of atmospheric water amounts only to a very small percentage of the total water.

With the development of faster and more robust in-situ measurement methods for water vapor isotopologues, the number of measurements has been strongly increasing in the last years. Available techniques include tunable diode laser (TDL) absorption spectroscopy (Lee et al., 2005), in-situ FTIR (Fourier Transform Infrared) (Griffith et al., 2006), cavity ringdown spectroscopy (Gupta et al., 2009) and integrated cavity output spectroscopy (Wang et al., 2009; Sturm and Knohl, 2010). These techniques are now operational at several ground sites and has been installed on mobile platforms like balloons, ships, and aircraft. In addition, the ground-based FTIR remote sensing observations are made within MUSICA/NDACC (MUltiplatform remote Sensing of Isotopologues for investigating the Cycle of Atmospheric water/Network for the Detection of Atmospheric Composition Change, Schneider et al., 2006, 2012) and TCCON (Total Carbon Column Observing Network, Wunch et al., 2010) networks.

In addition, global water isotopologue data have become available using remote sensing techniques installed on-board satellite platforms: the Interferometric Monitor for Greenhouse Gases (IMG) on ADEOS (Zakharov et al., 2004; Herbin et al., 2007), the Tropospheric Emission Spectrometer (TES) on Aura (Worden et al., 2006), the Michelson Interferometer for Passive Atmospheric Sounding (MIPAS) on Envisat (Payne et al., 2007; Steinwagner et al., 2007, 2010; Lossow et al., 2011), the SCanning Imaging

AMTD
7, 9095–9135, 2014

Absorption spectroMeter for Atmospheric CHartography (SCIAMACHY) on Envisat (Frankenberg et al., 2009; Scheepmaker et al., 2013), the Infrared Atmospheric Sounding Interferometer (IASI) on Metop (Herbin et al., 2009; Lacour et al., 2012; Schneider and Hase, 2011; Wiegele et al., 2014), and the Greenhouse gases Observing SATellite (GOSAT) launched by the Japanese Space Agency in January 2009 (Boesch et al., 2013; Frankenberg et al., 2013). These instruments are sensitive to different parts of the atmosphere. For example, MIPAS has high sensitivity in the upper troposphere and stratosphere as it is a limb thermal infrared sounder, TES is a nadir-looking thermal infrared sounder with high sensitivity from 850 hPa to 500 hPa (version 4) or from 900 to 425 hPa (version 5), while SCIAMACHY has high sensitivity throughout the column down to the surface as it is a nadir looking short-wave infrared (SWIR) sensor. The sensitivity of the retrieval to the true state of the atmosphere of these sensors is quantified by the averaging kernel (AK).

Adequate tools to investigate and use these global scale water isotopologue measurements are isotope-enabled atmospheric general circulation models (Iso-AGCMs), such as: ECHAM (Hoffmann et al., 1998), GISS-E (Goddard Institute for Space Studies, Schmidt et al., 2005), MUAGCM (Melbourne University General Circulation Model, Brown et al., 2006), IsoGSM (Isotopes-incorporated Global Spectral Model, Yoshimura et al., 2008), and LMDZ iso-GCM (the Laboratoire de Météorologie Dynamique atmospheric general circulation model with Zooming capability, Risi et al., 2010). These models integrate the well-known fractionation physics in the model's hydrological cycle. The main objective of water isotope studies is to test the parameterization of the hydrological cycle in AGCMs with isotope data as an independent and sensitive tracer of the model's hydrology. Several studies demonstrated that these climate models could simulate the isotopic composition of meteoric water quite realistically compared with measurements in precipitation from the GNIP network (Hoffmann et al., 1998; Noone and Simmonds, 2002; Schmidt et al., 2007; Yoshimura et al., 2008).

In recent years, several studies have been carried out to investigate the use of new datasets of water isotopes retrieve from satellite measurements. Frankenberg

AMTD
7, 9095–9135, 2014

et al. (2009) compared the SCIAMACHY HDO measurements with the IsoGSM model. Yoshimura et al. (2011) extensively compared the HDO measurements from SCIAMACHY, and TES version 4 with IsoGSM results, Risi et al. (2012a) conducted an inter-comparison study between models and observations, both ground-based and from satellites. Recently Frankenberg et al. (2013) compared GOSAT with LMDZ model outputs.

When comparing satellite data with model results, the sensitivity of the satellite sensor to the different layers of the atmosphere has to be taken into account. For example, the TES_{V4} dataset is sensitive only to a limited altitude range (mid troposphere, 850–500 hPa), in order to reduce the impact of non-linearities within the retrieval process (Worden et al., 2006). Therefore TES_{V4} is not sensitive to humidity and isotopologues in the lower troposphere. A low sensitivity means that the measured signal receives a low weight in the retrieval compared with the a priori assumed profile.

The retrieval process provides us with a quantitative measure of how much the a priori profiles have been modified by the actual satellite observations, i.e. the averaging kernel (AK). For a meaningful satellite-model comparison, the retrieval's AK must be applied to the model. The principle of applying an AK to the model output can be formulated as: $X_{GCM}^{New} = X_a + A[X_{GCM} - X_a]$, where A is the averaging kernel vector obtained from the satellite retrieval, X_a is a priori information that is used for the satellite retrieval and XGCM is the original model field. If the satellite retrieval represents the atmospheric conditions perfectly (AK = 1), applying the AK has no effect on the model results. On the other hand, if the sensitivity of the satellite retrieval is small and thus the AK is low, applying the AK to the model will yield the a priori profile (as does the measurement in this case). Here, we compare the TES version 4 and 5 datasets to the ECHAM4 model output, which was convoluted with the respective AK of the two retrieval versions. Moreover, the results are compared with data from SCIAMACHY, which has high sensitivity near the surface. The focus of this paper is to establish to what degree the different datasets reproduce several well-established isotope signals (temporal and spatial variations).

AMTD
7, 9095–9135, 2014

The paper is organized as follows. In Sect. 2 we describe the SCIAMACHY, TES version 4 and 5 datasets, and the ECHAM4 model. The SCIAMACHY and TES δD products are fundamentally different. For SCIAMACHY, the δD total column is calculated from the retrieved HDO and H_2O columns while for TES, the δD is very close to an optimal estimation product calculated from the spectral radiances. In Sect. 3 we describe several well-known isotopic effects of water vapor. In Sect. 4 we compare the remote sensing δD datasets with each other and with the model results. In particular we discuss the consequences of applying the AK from both TES versions to the ECHAM4 model output. Conclusions are presented in Sect. 5.

2 Instruments and methods

2.1 SCIAMACHY data

The SCIAMACHY instrument aboard the European Space Agency (ESA) environmental research satellite ENVISAT measured between 2003 and 2012 near short-wave infrared spectra, which allows the retrieval of total column abundances of H_2O and HDO (Frankenberg et al., 2009; Scheepmaker et al., 2013). SCIAMACHY has high sensitivity throughout the column down to the surface. The SCIAMACHY spectrometer has relatively high spectral resolution (0.2 nm to 0.5 nm) and covers a wide wavelength range (240 nm to 1700 nm and 2000 nm to 2400 nm) with an apodized spectral resolution of 0.85 cm^{-1}, which enables SCIAMACHY to detect many different gases, clouds and aerosols. In addition, SCIAMACHY has three different viewing geometries, which are nadir, limb and sun/moon occultation. HDO data were retrieved from nadir measurements using a narrow wavelength interval from 2355 to 2375 nm (Frankenberg et al., 2009). The footprint area of an individual HDO measurement is 120 km × 30 km. HDO data used in this study are temporally averaged from 2003 to 2005. Detailed information about the retrieval procedure and data processing can be found in Frankenberg et al. (2009) and Scheepmaker et al. (2013).

AMTD
7, 9095–9135, 2014

2.2 TES data

The Tropospheric Emission Spectrometer (TES) aboard the Aura satellite is an infrared Fourier Transform Spectrometer (FTS), which measures the spectral infrared (IR) radiances between 650 and 3050 cm^{-1} in the limb and a nadir viewing mode. HDO and H_2O abundances were obtained from TES thermal radiances between 1200 and 1350 cm^{-1} (7400 to 8300 nm in wavelength) with an apodized spectral resolution of 0.1 cm^{-1} for the nadir view. The footprint is 5.3 km × 8.4 km in the nadir-viewing mode. In this configuration, TES provides vertical information of abundant atmospheric species, such as O_3, CO, CH_4, H_2O and HDO (Worden et al., 2006). For the version 4 dataset, weighted mean values of the isotopic composition were provided for the height interval 500 to 850 hPa, where the HDO measurements have the highest sensitivity. Detailed information about TES data in general and the TES water isotopologue dataset can be found in Worden et al. (2004, 2006, 2007).

The TES retrieval version 5 has an improved sensitivity near the surface and covers the altitude range from 900 to 425 hPa (Worden et al., 2012). The TES version 5 data product is different from version 4 in many aspects, for example the aggregation of data by month, the reduced data size, the application of known corrections through validation campaigns, and the combination of all necessary meta-data in ancillary and multiple TES product files. The data used in this study are TES data measured in 2006 for both versions when TES had good spatial and temporal resolution. Filtering procedures have been applied to both versions with the same criteria, such as Degree Of Freedom signal, DOF > 0.5 and Species Retrieval Quality, SRQ = 1, in order to have an equal comparison.

2.3 The ECHAM4 model

The ECHAM atmospheric GCM was developed at the Max-Planck Institute for Meteorology in Hamburg. The ECHAM4 version used in this study was run with a spatial resolution of 2.8° by 2.8° (spectral resolution T42), with a vertical sigma-pressure hybrid

AMTD
7, 9095–9135, 2014

resolution of 19 layers. The ECHAM model uses a semi-Lagrangian advection scheme for both active tracers (e.g. moisture and cloud liquid water) and passive tracers (e.g. moisture and cloud water isotopologues). A detailed description of the incorporated water isotope physics can be found in Hoffmann et al. (1998). We note that the model considers fractionation effects at the surface only during evaporation from interception water and snow, however not from bare soil. Like other Iso-AGCMs, ECHAM distinguishes two types of fractionation processes: equilibrium and non-equilibrium fractionation. Equilibrium evaporation/condensation is a result of the different partial pressures of the water isotopologues and its description in the model is straightforward. Non-equilibrium effects play a major role during evaporation from open water (i.e. the oceans), during evaporation from falling raindrops below the cloud base and during ice crystal formation in an oversaturated environment. Its parameterization within the model is based on the different molecular diffusivities.

In the ECHAM results discussed here, the model wind fields were nudged to observational data (ERA40, Uppala et al., 2005). The ECHAM data used in this study correspond to the year 2001. Details of the satellite data and the model are summarized in Table 1.

2.4 Data processing

2.4.1 Unit

All HDO data from observations and model are presented as deviation (delta deuterium, δD) from the isotopic composition of the international standard Vienna Standard Mean Ocean Water (VSMOW, Craig, 1961) expressed in per mill (‰):

$$\delta = \frac{R_{\text{sample}}}{R_{\text{VSMOW}}} - 1 \tag{1}$$

R_x refers to the D/H ratio of the sample and of the reference material, respectively. Due to the low abundance of D, this is very similar to the observed and modeled

AMTD
7, 9095–9135, 2014

isotopologue ratio HDO/H_2O, which is retrieved by the satellite and modeled in the model, and the differences between the two are negligible for our study. Positive δ values indicate an enrichment of deuterium in the sample compared to the VSMOW standard, while negative values indicate depletion of D.

Since the water vapor mixing ratio and δD decrease with altitude, the total column value of δD is calculated as a weighted mean:

$$\overline{\delta D} = \frac{\sum_{i=0}^{n} (\delta D_n \cdot H_2O_n)}{\sum_{i=0}^{n} H_2O_n} \quad (2)$$

Where n is the number of layers. All results are given as weighted means ($\overline{\delta D}$).

2.4.2 Application of satellite averaging kernel to model results

In order to compare the model results to satellite observations, the ECHAM model output was convoluted with the averaging kernel from the TES satellite datasets. Unlike for real atmospheric observations, in the model the "true state" is explicitly available. By applying the AK to the model results we mimic the way in which the satellite observes the atmosphere, to allow a meaningful comparison with the model.

The TES data were interpolated on the horizontal grid of the model, while in the vertical the model was interpolated on the TES layers. One should note that the AK convolution must account for the cross correlations in the joint HDO/H_2O profile retrieval (Yoshimura et al., 2011; Worden et al., 2006, 2011). The basic application of the AK to the model is presented in Eqs. (3) and (4). These equations can be re-formulated into Eq. (5) for the HDO/H_2O ratio, and to Eq. (6) for H_2O (see also Supplement of Risi

AMTD
7, 9095–9135, 2014

et al., 2013).

$$\mathrm{ECHAM}_{\mathrm{AK}} = X_{\mathrm{a}} + A_{\mathrm{TES}}[X_{\mathrm{m}} - X_{\mathrm{a}}] \quad (3)$$

$$A_{\mathrm{TES}} = \begin{bmatrix} A_{\mathrm{DD}} & A_{\mathrm{DH}} \\ A_{\mathrm{HD}} & A_{\mathrm{HH}} \end{bmatrix} \quad (4)$$

$$\ln\left(\mathrm{ECHAM}^{\mathrm{R}}_{\mathrm{AK}}\right) = \ln(R_{\mathrm{a}}) + \left((A_{\mathrm{DD}} - A_{\mathrm{HD}}) \cdot \ln\left(\frac{R_{\mathrm{m}}}{R_{\mathrm{a}}}\right) + (A_{\mathrm{DD}} - A_{\mathrm{HD}} - A_{\mathrm{HH}} + A_{\mathrm{DH}}) \cdot \ln\left(\frac{q_{\mathrm{m}}}{q_{\mathrm{a}}}\right)\right) \quad (5)$$

$$\mathrm{ECHAM}^{\mathrm{H}}_{\mathrm{AK}} = X^{\mathrm{H}}_{\mathrm{a}} + A_{\mathrm{HH}}\left(X^{\mathrm{H}}_{\mathrm{m}} - X^{\mathrm{H}}_{\mathrm{a}}\right) + A_{\mathrm{HD}}\left(X^{\mathrm{D}}_{\mathrm{m}} - X^{\mathrm{D}}_{\mathrm{a}}\right) \quad (6)$$

D and H stand for HDO and H_2O, respectively while m and a stand for the model field and the a priori field, respectively. R is the ratio of volume mixing ratios of HDO and H_2O (i.e. $R_{\mathrm{a}} = (\mathrm{HDO}/\mathrm{H_2O})$ of TES a priori). q is the specific humidity; A_{DD} and A_{HH} are the averaging kernel sub-matrices for HDO and H_2O; A_{HD} and A_{DH} are the cross correlation AK matrices between H_2O and HDO and the reverse (see also Worden et al., 2006; Yoshimura et al., 2011; Risi et al., 2013). $\mathrm{ECHAM}^{\mathrm{R}}_{\mathrm{AK}}$ is the new $\mathrm{HDO}/\mathrm{H_2O}$ ratio R as a function of pressure grid for the convoluted ECHAM.

The application of the averaging kernel to the model output has two components (see Eq. 5). The first depends on the difference between the a priori $\mathrm{HDO}/\mathrm{H_2O}$ ratio profile and the model $\mathrm{HDO}/\mathrm{H_2O}$ ratio profile. The second depends on the difference between the a priori humidity profile and the model humidity profile. If there is a model bias in humidity, the difference between model humidity and a priori humidity will affect the model-data comparison of δD. The model humidity bias commonly occurs in the upper troposphere, also in the ECHAM model. This bias may then be propagated to the lower-tropospheric δD through the averaging kernels (Worden et al., 2012; Risi et al., 2013). The effect of the model humidity bias can be eliminated by assuming that the model captures correctly the satellite a priori humidity profile. Based on this

AMTD
7, 9095–9135, 2014

assumption, the second component in Eq. (5) can be neglected.

$$\ln\left(\mathrm{ECHAM}^{\mathrm{R}}_{\mathrm{AKBcorr}}\right) = \ln(R_{\mathrm{a}}) + \left((A_{\mathrm{DD}} - A_{\mathrm{HD}}) \cdot \ln\left(\frac{R_{\mathrm{m}}}{R_{\mathrm{a}}}\right)\right) \quad (7)$$

Schneider et al. (2012) discussed the complexity of HDO and humidity retrieval from satellite datasets in detail. They introduce an a posteriori processing method to take into account the cross dependence of retrieved δD on atmospheric humidity. The aim is to get similar AKs for HDO and H_2O since the variability in the ratio of water vapor isotopologues is much smaller than the variability of humidity (Schneider et al., 2012; Pommier et al., 2014; Wiegele et al., 2014). When the AKs are similar, the retrieved isotopologue ratio and humidity are sensitive to the same atmospheric air mass and the cross dependence of atmospheric humidity on the retrieved δD is significantly reduced.

In the case of SCIAMACHY, we do not apply the AK's to the model, since the AK for SCIAMACHY measurements is close to unity throughout the entire column and does not vary in time and space (Frankenberg et al., 2009; Yoshimura et al., 2011).

2.4.3 Bias correction

A bias of ~ 5 % on average and ~ 15 % maximum in the TES HDO vapor data has been attributed to uncertainties in the spectroscopic line strengths (Worden et al., 2006, 2007, 2011). A correction for this bias is already included in the version 5 dataset (Worden et al., 2012) but not in version 4. The sensitivity of the measurements must be accountd for in the application of the bias correction to the $\mathrm{TES}_{\mathrm{V4}}$ data (Lee et al., 2011; Risi et al., 2013) according to:

$$X^{\mathrm{HDO}}_{\mathrm{corrected}} = X^{\mathrm{HDO}}_{\mathrm{original}} - A_{\mathrm{DD}}(\delta_{\mathrm{bias}}) \quad (8)$$

$X^{\mathrm{HDO}}_{\mathrm{corrected}}$ is the logarithm of the volume mixing ratio of the HDO profile after bias correction, $X^{\mathrm{HDO}}_{\mathrm{original}}$ is the logarithm of the original volume mixing ratio of the model or satellite,

AMTD
7, 9095–9135, 2014

and δ_{bias} is a column vector of the same length as $X^{HDO}_{original}$ that contains the bias correction values. Note, that this correction is only applied to HDO and not to H_2O. We applied the bias corrections of 5 % to TES_{V4} (Worden et al., 2006) and no bias correction was applied to TES_{V5} since it has already been corrected by 6.5 % (Worden et al., 2012). In order to have a good agreement amongst the data in the tropic, bias corrections of 3 % and 5 ‰ were applied to $ECHAM_{AK4}$ and SCIAMACHY.

3 The isotopic effects

Before presenting the results of our study, we briefly summarize the most important spatial and temporal isotope features and their underlying mechanisms. We focus in the following on δD; similar arguments hold for $\delta^{18}O$.

Since the start of water isotopologue studies in the 60s (Dansgaard, 1964) a number of empirical relationships between the isotopic composition of precipitation and several geographical or climatological parameters have been established. The principal "isotopic effects" such as the temperature effect, the amount effect, the altitude effect and the latitudinal effect will be used in the following to make a first order evaluation of the satellite data and the model results. The temperature effect denotes the spatial relationship between annual (or monthly or seasonal) mean temperatures and δD of the respective precipitation (i.e. annual or monthly or seasonal mean). A linear relationship holds over a wide temperature range. The altitude effect and the latitudinal effect denote linear relationships between δD and these geographical quantities. Since both quantities, i.e. altitude and latitude, correlate strongly with temperature, both effects are partly a direct consequence of the spatial temperature effect. However, there are some mechanisms involved that are independent of temperature. For instance, the triggering of strong convective activity next to orographic obstacles contributes to the altitude effect.

In the tropics (latitudes $< \pm 15^{\circ}$), the linear relation between surface temperatures and δD becomes less apparent. More frequent convectively formed precipitation and

AMTD
7, 9095–9135, 2014

thus more vertical air movement seem to disturb the control of the temperature effect. However, in particular in tropical and subtropical regions, a relation between the amount of precipitation and δD (the amount effect) appears in the data for which a full explanation is still under debate (Dansgaard, 1964; Aggarwal et al., 2007; Risi et al., 2008). Another geographical isotope effect is the continental effect. Along their trajectory across large continental land masses air is becoming disconnected from the oceanic water supply to compensate for the successive rain events. This leads again to a distillation effect with the heavier isotopes being progressively removed from these travelling air masses. The continental effect is therefore also related to the temperature effect, but adds an additional mechanism to the purely temperature controlled rainout processes. It is particularly pronounced along principal air mass trajectories, e.g. from the Gulf of Mexico into the Southwest of the United States or from the North Atlantic into Western and Central Europe.

4 Results and discussion

4.1 Spatial isotope distribution

The annual mean δD isotope distributions of the different satellite and model datasets and the TES prior are shown in Fig. 1. The TES prior profiles as an initial guess for HDO and H_2O used to constrain the HDO/H_2O estimation does not show a latitudinal effect (Fig. 1a). The TES prior for HDO (HDO_{prior}) was calculated based on an estimated atmospheric H_2O profile from re-analysis data, multiplied by a single a priori profile of the HDO/H_2O ratio, which was obtained from a run of the National Center for Atmospheric Research (NCAR) Community Atmosphere Model (CAM), augmented with an isotope physics approach developed by Noone and Simmonds (2002) (Worden et al., 2006, 2012; Zhang et al., 2010). This prior HDO profile is representative for the tropical HDO/H_2O ratio and as a result, the TES δD prior is strongly biased high at high latitudes. The TES prior does include an altitude effect (Fig. 1a), which is clearly

AMTD
7, 9095–9135, 2014

visible in the Himalayas, the Andes, the Rocky Mountains, and Greenland. The prior for TES version 5 is not significantly different from version 4.

The SCIAMACHY prior shows the same pattern as the TES prior (Fig. 1i) but generally lower δD values of −140 to −160 ‰. It does not include a latitudinal gradient and altitudinal effect. The sensitivity to the weak HDO absorber is close to unity throughout the column (Frankenberg et al., 2009; Scheepmaker et al., 2013). Unlike TES, the SCIAMACHY prior was constructed from ECMWF water vapor profiles and a fixed prior depletion profile. We assume −100 ‰ at the lowest layer and it increases to −500 ‰ at the highest layer. This results the prior total column δD value of approximately −150 ‰.

Figure 1b–h and j presents modeled and observed patterns (isoscapes) of total column δD of atmospheric water vapor. The first order isotope feature shown in all figures is the significant difference in δD between low, mid and high latitudes roughly following global temperatures. The latitude effect is stronger in the observed global isotope pattern of the TES version 5 (TES_{V5}) and of the SCIAMACHY dataset than in the TES version 4 (TES_{V4}). It is also present in the modeled results of ECHAM. ECHAM results convoluted with the AK of TES version 4 ($ECHAM_{AK4}$) shows a smaller latitude gradient than for version 5 ($ECHAM_{AK5}$). Another feature, visible in these global isoscapes, is the tropical and sub-tropical zones with enriched values are wider in the ECHAM model results (Fig. 1b, e, f, h, j) compared to the TES_{V5} and SCIAMACHY satellite observations (Fig. 1d and g).

A strong latitude effect of the order of ∼ 150 ‰ for δD between the tropics and the cold and isotopically depleted polar regions of both hemispheres is well established in the literature. Isoscapes based on an interpolated multi-variable regression of GNIP precipitation data show strong latitudinal gradients (Bowen and Wilkinson, 2002). Also the few existing near surface vapor measurements (Uemura et al., 2008) indicate a strong isotopic gradient between low and high latitudes. This principal geographical pattern is better represented in TES_{V5} compared to TES_{V4}, which has a stronger influence from the a priori field at higher latitudes. It clearly indicates a substantial improvement of the version 5 retrieval over version 4.

AMTD
7, 9095–9135, 2014

The altitude effect is apparent in all datasets. Major mountain chains such as the Andes, Rocky Mountains or the Himalayas together with the Tibetan Plateau are easily recognizable by lower δD values. ECHAM$_{AK5}$, however, is marked by unrealistically high δD values over the Tibetan plateau (Himalayas; Fig. 1f). This unrealistic pattern is due to a high bias in the model humidity profile as discussed in Sect. 2.4 (Risi et al., 2012b, 2013) and the effect of limited vertical resolution and a priori constraints on retrieved δD over the Himalaya region. Therefore, this problem disappears when we leave out the humidity term in the application of the AK (Eq. 7), and the resulting ECHAM$_{AK5BCorr}$ shows a local isotope minimum over the Tibetan Plateau again (Fig. 1h). Thus, the humidity bias can have a large effect on the isotope results of a model convoluted with the averaging kernel of a satellite instrument.

The unrealistically high δD values over the Tibetan plateau also disappear if we perform the a posteriori analysis suggested by Schneider et al. (2012); Pommier et al. (2014) (Eqs. 16 and 17) (Fig. 1j). The a posteriori data treatment results δD and H_2O profiles that are sensitive to the same atmospheric airmass. As a result, the AK application to the model with applied a posteriori analysis produces a similar result as the humidity correction (Fig. 1h and j). Latitudinal profiles from both ECHAM$_{AK5Corr}$ and ECHAM$_{AK5Pos}$ show very similar δD values in the tropics and only 2–5 ‰ differences at the higher altitudes (figure not shown). Both correction procedures thus show that humidity biases have to be taken into account when the satellite AKs are applied to model results, either by a humidity correction or an a posteriori processing. Since the results from ECHAM$_{AK5Corr}$ and ECHAM$_{AK5Pos}$ are similar, we only plotted the results of ECHAM$_{AK5Corr}$ for the rest figures.

The isotopically most enriched regions of the atmosphere are situated over tropical South America and tropical Africa and are associated with the Amazon and Congo River basins. The location and extension of these maxima are relatively robust throughout all datasets. Since these large areas with δD between −95 and −80 ‰ are not apparent in the TES and SCIAMACHY a priori fields (Fig. 1a and i) but clearly appear in the final product (Fig. 1c, d, and g), they are a robust result of the added information

AMTD
7, 9095–9135, 2014

from the satellite measurements and not an artificial product of the retrieval procedure. The intense recycling and very strong evapo-transpiration over these rainforest regions is responsible for this pattern (Worden et al., 2007; Yoshimura et al., 2011).

In the scientific literature, many examples of the continental effect are documented, e.g. the Southwestern US or Western/Central Europe, based on measurements in ground waters (Rozanski, 1985) and precipitation (Aggarwal et al., 2007). The continental effect appears in all datasets with varying intensity, except for ECHAM convoluted with AK version 4. TES_{V4}, TES_{V5}, SCIAMACHY, ECHAM, $ECHAM_{AK5}$, $ECHAM_{AK5Corr}$, and $ECHAM_{AK5Pos}$ results clearly show the continental effect (white arrows in Fig. 1d).

The Hadley-Walker Circulation defines the seasonally varying zones of strong convective activity in the tropics. Three rising branches of the meridional Walker circulation are situated over tropical South America, tropical Africa and the Western Pacific Warm Pool (Oort and Yienger, 1996). As described above, the strong enrichment over the continental parts of the Walker circulation is due to the intense recycling of continental water there. However, over the Pacific warm pool one recognizes a zone with slightly more depleted δD (ellipses in Fig. 1b, d, f, g, and h). This area of very high Sea Surface Temperature (SST), strong convection and rainfall and more depleted vapor extends over the Inner Tropics and is surrounded by a zone of descending air, less rainfall (Oort and Yienger, 1996; Jo et al., 2014) and more enriched vapor. We consider this pattern as a manifestation of the isotopic amount effect since the isotopic pattern anti-correlates with regional rainfall (Brown et al., 2008; Dansgaard, 1964; Kurita et al., 2011; Lee and Fung, 2007; Lee et al., 2011; Risi et al., 2008; Worden et al., 2007). Apparently, TES_{V4} and $ECHAM_{AK4}$ (Fig. 1c and e) do not pick up this important feature of the tropical water cycle.

Figure 2 presents a comparison of zonal mean δD values for all datasets. As discussed above, δD decreases to −200 ‰ in the TES_{V4} product at high northern latitudes, whereas it decreases to −250 ‰ for TES_{V5}, the latter in agreement with SCIAMACHY, and with other independent observations (Uemura et al., 2008). TES_{V4}

AMTD
7, 9095–9135, 2014

displays much weaker δD gradients at mid latitudes compared to SCIAMACHY and TES_{V5}. As mentioned earlier, the tropical and sub-tropical isotope maximum in the ECHAM model is significantly wider than for SCIAMACHY and TES_{V5} (Fig. 2b). This issue is aggravated when the ECHAM results are convoluted with the TES averaging kernels. The $ECHAM_{AK4}$ product shows the smallest latitude gradient and highest δD values at high latitude of all datasets. The small AK values of version 4 enhance the influence of the a priori field, which consequently leads to more enriched δD values. This high-latitude problem has been improved in the version 5 datasets (Fig. 2b), but still the $ECHAM_{AK5}$ and $ECHAM_{AK5Corr}$ results are significantly higher than the model state of ECHAM at northern high latitudes. TES_{V5} is in good agreement with SCIAMACHY.

A main reason for the improvement of TES_{V5} latitude gradient is the greatly increased in sensitivity. The increased number of radiance measurements used for retrieval and the changed of both the hard constraints (e.g. retrieval levels and mapping matrices) and the soft constraints (e.g. constraint matrix) in the version 5 dataset improve the TES_{V5} sensitivity (Worden et al., 2012). A good indicator for retrieval sensitivity is the DOF (Degree Of Freedom) satellite as it shows how well the satellite captures the range of variability of the true distribution. There are many version 5 datasets at higher latitudes that pass the applied DOF criteria (see Fig. 5 in Worden et al., 2012). Therefore, version 5 represents better the true natural variability of atmosphere at higher latitudes than version 4.

Although, there are significantly discrepancies at mid and high latitudes, all data products agree fairly well in a tropical/subtropical band between 30° N and 30° S with values around −100 ‰, similar to Webster and Heymsfield (2003), Lawrence et al. (2004) and Zakharov et al. (2004). It seems therefore that different remote sensing datasets and model results (with AK applied) coincide in the tropics, which mean that the isotope measurements there can be exploited to examine smaller scale effects (see below).

AMTD
7, 9095–9135, 2014

4.2 Temporal isotope distribution

Above we analyzed the spatial structure of the dominant annual average isotope patterns. In addition, both satellite data and model simulations allow us to study the seasonality of δD patterns and to identify the leading processes on this time scale. Zonal means of all datasets are computed for the mean winter (DJF) and summer season (JJA) of the respective annual time period (Fig. 3). TES_{V5} shows similar results as SCIAMACHY during summer and winter in the Northern Hemisphere and both datasets show a clear and consistent seasonal isotope difference between the two seasons in the Northern Hemisphere. In the Southern Hemisphere, however, the difference between the two seasons is much smaller for both datasets. In addition, in the Southern Hemisphere there appears to be a significant difference between the instruments. TES_{V5} δD values are consistently lower compared to SCIAMACHY (Fig. 3a).

Due to the high solar zenith angle (low sun), SCIAMACHY data are seasonally scarce at mid and high latitudes. Therefore, there are not many measurements above 50° N or 50° S in the respective winter season (Fig. 3a). Also, large parts of the oceans are not covered due to the low albedo of the ocean; therefore the signals from oceanic regions are primarily caused by reflection on low-level clouds. In the SCIAMACHY retrieval, a data filter is applied, which only accepts water isotopologue measurements if the H_2O total column corresponds to at least 70 % of the ECMWF total water column (Frankenberg et al., 2009). This constraint excludes profiles with high clouds, but accepts profiles with low clouds (up to 1 km). Thus all SCIAMACHY measurements are biased towards clear sky or low cloud conditions. The δD seasonality of SCIAMACHY shown in Fig. 3a (especially in the Southern Hemisphere during the Northern Hemisphere Summer) is therefore neither temporally nor spatially fully representative of the mean state of the atmosphere. These issues are not applicable to TES data. However, TES measurements are also less sensitive at higher latitudes, especially the version 4 dataset.

AMTD
7, 9095–9135, 2014

The wider tropical maximum of ECHAM is seen in both seasons (Fig. 3b). It is apparent that in the summer season the $ECHAM_{AK5}$ results show considerably higher δD values than TES_{V5} in the Northern Hemisphere and it is vice versa for the winter season in the Southern Hemisphere. This shows that the annual bias in ECHAM as discusses above originates to a large degree from the summer season. The mid latitudinal bias found in the ECHAM model is a common bias that is present in many GCM models. In general, most GCM models tend to overestimate humidity in the tropics and subtropics due to the inadequate representation of cloud processes or of the large-scale circulation, or to excessive diffusion during the transport of water vapor (Risi et al., 2012a, b). The overestimation of humidity in the subtropic affects the enrichment of δD in the mid and high troposphere.

Whereas there are still some discrepancies between the different data products at mid and high latitudes, isotope data within a zonal band from 30° N to −30° N are roughly consistent, both for the annual average and the summer and winter profiles. An interesting feature of all datasets except for TES_{V4} (not shown) is a seasonal seesaw behavior of the latitudinal δD profiles in the inner tropics: in both seasons, the δD values close to the equator are lower in the respective summer hemisphere than in the winter hemisphere. The absolute δD variations are small and extend over different ranges in the respective hemispheres, but the δD latitude profiles for the two seasons (solid and dashed lines of each color) intersect very close to the equator.

This seasonal variation of δD in the tropics is a robust feature of the TES_{V5} dataset and a consequence of the seasonal displacements of the ITCZ (Inter Tropical Convergence Zone). Tropical rainfall bands and corresponding convective activity closely follow the maxima of insolation. The ITCZ is displaced towards the north during Northern Hemisphere summer and towards the south during Southern Hemisphere summer. Due to the isotopic amount effect, we expect the convectively active regions within the ITCZ to be associated with lower δD values. Therefore, areas north (south) of the equator are isotopically more (less) depleted during NH summer, and vice versa during NH winter. The isotopic amount effect therefore leads to the seesaw behavior of the zonal

AMTD
7, 9095–9135, 2014

δD means where the latitudinal profiles in the two seasons have their lower values in the summer hemisphere (see the crossing lines in Fig. 4). This seesaw behavior has already been recognized in precipitation data (Waliser and Gautier, 2010; Wu et al., 2003; Back and Bretherton, 2005).

SCIAMACHY and TES_{V5}, show this isotope feature with varying intensity (Fig. 4a). The amount effect due to the movement of ICTZ is more pronounced in SCIAMACHY than in TES_{V5}. The original ECHAM model and $ECHAM_{AK5Corr}$ also show this seesaw pattern (Fig. 4b).

A possible reason why SCIAMACHY shows this seesaw pattern more clearly is SCIAMACHY's higher sensitivity at lower altitudes where many processes contributing to the amount effect occur (such as re-evaporation of raindrops in more/less humid air, etc). In order to investigate this further, we separated ECHAM, TES_{V5}, and $ECHAM_{AK5Corr}$ into two layers (Fig. 5). Figure 5b confirms that seesaw pattern in the TES_{V5} originates from the lower layer. This is qualitatively in line with the fact that SCIAMACHY is sensitive down to the surface and the seesaw pattern nicely shows up in the SCIAMACHY dataset. We note that this was not necessarily expected since the seesaw phenomenon is largely produced by displacements of the ITCZ over the oceans, where the SCIAMACHY coverage is relatively low (due to the requirement of low-level clouds) compared to the coverage over land. In contrast, ECHAM and $ECHAM_{AK5Corr}$ show the seesaw pattern throughout the entire atmospheric column, both at the lower and high layers (Fig. 5a and c). It seems that the model overestimates the correlation between lower and higher layers than the observations. It was speculated that GCMs in general show strong coherence between processes at lower altitudes (such as Sea Surface Temperature variations) and associated features at high altitudes (such as high convective cloud formation). In this case the common isotope seasonality at low and high altitudes in the model might be a further consequence of these known model problems (Risi et al., 2012a; Conroy et al., 2013). The representation of this "fine structure" is an important feature, which needs further investigation in remote sensing datasets of water isotopologues. It should be noted that the cloud height issue might cause the

AMTD
7, 9095–9135, 2014

seesaw pattern seen in the satellite datasets. Satellites in general measure the δD values above the clouds, which means during convection the satellite data will represent δD at high altitudes where δD is lower.

4.3 Relation of water vapor and δD

Already in 1964, Dansgaard (1964) described the global water cycle as a Rayleigh-type distillation model. Each condensation process extracts a certain quantity of water from an air mass, when it moves from its tropical/subtropical source regions to higher latitudes. Assuming that this process is exclusively temperature dependent and controlled by a moist adiabatic lapse rate one can simply quantify the isotopic temperature effect over a wide temperature range. It is instructive to check to what degree the atmosphere corresponds to this simple temperature dependent scheme: how Rayleigh-like is the earth's atmosphere?

Decreasing temperatures from the surface to higher altitudes dry the corresponding air and lead to both lower total precipitable water (TPW), and via the Rayleigh mechanism, to more depleted isotope values. In a pure Rayleigh distillation system, $\ln(HDO/H_2O)$ is linearly related to ln(TPW) and the slope corresponds to the effective equilibrium fractionation, $\alpha_{eff} - 1$ (Frankenberg et al., 2009; Schneider et al., 2010; Yoshimura et al., 2011). Here, α_{eff} refers to a mean fractionation over the entire distillation process with an "effective fractionation temperature" (Frankenberg et al., 2009; Yoshimura et al., 2011).

In the following we investigate whether the atmosphere follows such a Rayleigh distillation model. Globally, a $\ln(HDO/H_2O)$ vs. ln(TPW) plot (see Fig. 6a and b) is dominated by the latitudinal gradient of both quantities (i.e. the latitude effect). Lower ln(TPW) values and more depleted isotopic values are largely organized along a gradient from lower to higher latitudes. However, in the correlation plot also some clear deviations occur. At high ln(TPW) (> 3), the different datasets agree rather well, but bellow 3, significant differences become apparent. Between 2 and 3 ln(TPW), SCIAMACHY appears to have lower $\ln(HDO/H_2O)$ values than ECHAM and the TES. Below

AMTD
7, 9095–9135, 2014

2 ln(TPW), SCIAMACHY also displays a group of very high ln(HDO/H_2O) values, which show a larger scatter and deviate strongly from linear correlation. The ECHAM model shows two separated branches at the lower end of the global distillation chain, which corresponds to air-masses over Antarctica and the Arctic (Fig. 6b). This feature is not reproduced by any available observational dataset since observations are scarce in these regions.

It is evident that these structures influence the linear trend lines that are fit to the datasets and shown in Fig. 6. Steeper overall slopes are simulated for the original ECHAM model than observed by the satellite, because the model results include strongly depleted water vapor at higher latitudes, especially at Polar Regions, where no satellite data are available. TES_{V5} data results in a steeper slope than TES_{V4}, which again reflects the smaller latitude gradient in TES_{V4}, and convolution with the version 4 AK leads to a similarly low slope for $ECHAM_{AK4}$. The slope for the $ECHAM_{AK5}$ dataset is lower than TES_{V5}. However, both TES products disagree with ECHAM and SCIAMACHY for ln(TPW) lower than 2.5. The differences between datasets for lower ln(TPW) reflect the differences discussed in Sect. 4.1 for the latitudinal δD gradients at mid and high latitudes. In the following we focus on the tropical region (high ln(TPW)) where the latitudinal profiles agreed well.

In the tropics, the differences between the datasets in the ln(HDO/H_2O) vs. ln(TPW) correlation plot are smaller, but the correlation between ln(TPW) and the isotopes and the respective slope is lower also (Fig. 6c and d). This implies unrealistically high condensation temperatures for the satellite datasets (TES_{V5} and SCIAMACHY) and even more for the ECHAM model (up to almost 60 °C). Apparently, a description of the relatively small isotopic variance by a simple overall distillation process is hardly possible. This is likely due to the dominance of convective activity there, which affects the isotopic composition by many large scale (e.g. low level humidity confluence) and subscale processes (e.g. entrainment/detrainment of vapor in convective systems) that are not sufficiently described by Rayleigh fractionation. The isotope amount effect in

AMTD
7, 9095–9135, 2014

the tropics is another factor contributing to the relatively flat slope because it leads to lower δ values at higher humidity (Fig. 6d).

Figure 6e and f show ln(HDO/H_2O) vs. ln(TPW) from satellites and model simulations over the Sahel region (0–10° E, 15–30° N). The Sahel has been chosen because SCIAMACHY shows the best performance here and has recorded most measurements (> 6000 measurements, see Frankenberg et al., 2009). The slopes from all datasets in the Sahel are relatively flat except for SCIAMACHY. This may again be related to the vertical sensitivity. Based on a network of FTIR HDO/H_2O observations, Schneider et al. (2010) conclude that ln(HDO/H_2O) vs. ln(TPW) slopes are steeper in air masses close to the surface and decrease progressively with height. In our observations, the slope is highest for SCIAMACHY, with the highest sensitivity close to the surface. The slope is high for TES_{V4} and higher for TES_{V5}, which has the lowest sensitivity in the lower troposphere. Interestingly, the steeper slope from SCIAMACHY (0.093) is in the range of a typical Rayleigh distillation process slope, which is between 0.08–0.15 (+20 ∼ −20 °C) depending on evaporation/condensation temperatures (Majoube, 1971a, b; Yoshimura et al., 2011). The SCIAMACHY slope would correspond to an effective condensation temperature of 282 ± 7 K. The slopes from TES_{V5}, ECHAM and $ECHAM_{AK5}$ and $ECHAM_{AK5Corr}$ correspond to 314 ± 12 K, 318 ± 5 K, 314 ± 10 K, and 325 ± 5, respectively. These unrealistically high condensation temperatures imply that the atmosphere as a whole cannot be considered as a pure Rayleigh distillation column. In the atmosphere, there are many factors influencing this process such as mixing of the air parcel, evaporation of condensate water, kinetic effect, active convection (Gedzelman, 1988; Smith, 1992; Moyer et al., 1996; Keith, 2000; Galewsky et al., 2007). Apparently these processes have an important influence on the isotope-concentration correlations that overrule the condensation temperature-induced correlation.

AMTD
7, 9095–9135, 2014

5 Conclusions

Over the last years, water isotope retrievals have become available from different global satellite datasets. Here we compared the HDO/H_2O data from TES version 4, TES version 5, and SCIAMACHY with each other and with large-scale isotope patterns from the ECHAM model. We systematically assessed how first-order water isotope effects (temperature-, latitude-, altitude-, continental-, and amount-effect) are represented in the respective remote sensing datasets.

The geographical and temporal patterns in the respective water isotopologue fields reproduced the different "classical" large-scale isotope effects to a varying degree. Our analysis confirmed the improvement of TES_{V5} compared to TES_{V4} for the first-order global isotope signals investigated. Similarly, when the model results are convoluted with the AK, $ECHAM_{AK5}$ outperforms $ECHAM_{AK4}$. Nevertheless, we identified a problem with the $ECHAM_{AK5}$ results over the Himalayas region. The large positive isotope anomalies were shown to be caused by a high bias in humidity in ECHAM. A humidity correction or an a posteriori processing is necessary for model-data comparison because of cross dependence between H_2O and HDO in the application of the AK to the model. Furthermore, ECHAM overestimates δD values at mid latitudes compared to SCIAMACHY and TES_{V5} and the tropical and sub-tropical band of high δD values is wider in the model than in the satellite datasets. This is a common problem in many GCM models since the models tend to have a high moist bias in the tropical and sub-tropical regions associated with errors in cloud processes, large-scale circulation and diffusion during water vapor transport.

When examining the seasonally varying δD signal in the tropics associated to the movement of the ITCZ, SCIAMACHY, TES_{V5} and ECHAM showed the expected seasonal co-variation of the latitudinal δD minima and maxima in water vapor with insolation and rainfall. Some of the isotopologue effects are difficult to identify in SCIAMACHY because of its limited coverage of large parts of the respective winter hemispheres and oceans.

AMTD
7, 9095–9135, 2014

We also tested to what extent the atmosphere in the different datasets can be described as a Rayleigh distillation system. The results show that the atmosphere as a whole cannot be considered as a pure Rayleigh distillation column. For small region, e.g. in the Sahel, TES_{V5} and SCIAMACHY imply more Rayleigh type atmospheric processes than ECHAM. However, none of the effective condensation temperatures deduced from the observed slopes reflect pure Rayleigh condensation temperatures. This comes not as a surprise since many processes influence this condensation process, such as mixing of the air parcel, evaporation of condensate water, kinetic effect, and active convection, which are not controlled by a single effective condensation temperature.

One central application of existing and future water isotopologue datasets will be the evaluation of global observations and models. We suggest to use the qualitative and quantitative tests carried out in this study as a benchmark for the different data products and to evaluate their strengths and weaknesses.

Acknowledgements. This study was funded by NWO project number ALW-GO-AO/10-11 (the Netherlands Organization for Scientific Research). We thank M. Schneider for a very insightful and helpful review.

References

Aggarwal, P. K., Gat, J. R., and Froehlich, K. F. O.: Isotopes in the Water Cycle: Past, Present and Future of a Developing Science, Springer, IAEA, 2007. 9098, 9108, 9111

Back, L. E. and Bretherton, C. S.: The relationship between wind speed and precipitation in the Pacific ITCZ, J. Clim., 18, 4317–4328, 2005. 9115

Boesch, H., Deutscher, N. M., Warneke, T., Byckling, K., Cogan, A. J., Griffith, D. W. T., Notholt, J., Parker, R. J., and Wang, Z.: HDO/H_2O ratio retrievals from GOSAT, Atmos. Meas. Tech., 6, 599–612, doi:10.5194/amt-6-599-2013, 2013. 9099

Bowen, G. J. and Wilkinson, B.: Spatial distribution of $\delta^{18}O$ in meteoric precipitation, Geology, 30, 315–318, doi:10.1130/0091-7613(2002)030<0315:SDOOIM>2.0.CO;2v, 2002. 9109

AMTD
7, 9095–9135, 2014

Brown, J., Simmonds, I., and Noone, D.: Modeling $\delta^{18}O$ in tropical precipitation and the surface ocean for present day climate, J. Geophys. Res., 111, D05105, doi:10.1029/2004JD005611, 2006. 9099

Brown, D., Worden, J., and Noone, D.: Comparison of atmospheric hydrology over convective continental regions using water vapor isotope measurements from space, J. Geophys. Res., 113, D15124, doi:10.1029/2007JD009676, 2008. 9111

Conroy, J. L., Cobb, K. M., and Noone, D.: Comparison of precipitation isotope variability across the tropical Pacific in observations and SWING2 model simulations, J. Geophys. Res.-Atmos., 118, 5867–5892, doi:10.1002/jgrd.50412, 2013. 9115

Craig, H.: Isotopic variations in meteoric waters, Science, 133, 1702–1703, 1961. 9103

Dansgaard, W.: Stable isotopes in precipitation, Tellus, 16, 436–468, 1964. 9107, 9108, 9111, 9116

Ehhalt, D. H., Davidson, J. A., Cantrell, C. A., Friedman, I., and Tyler, S.: The kinetic isotope effect in the reaction of H_2 with OH, J. Geophys. Res., 94, 9831–9836, 1989. 9098

Frankenberg, C., Yoshimura, K., Warneke, T., Aben, I., Butz, A., Deutscher, N., Griffith, D., Hase, F., Notholt, J., Schneider, M., Schrijver, H., and Röckmann, T.: Dynamic processes governing the isotopic composition of water vapor as observed from space and ground, Science, 325, 1374–1377, doi:10.1126/science.1173791, 2009. 9097, 9099, 9101, 9106, 9109, 9113, 9116, 9118

Frankenberg, C., Wunch, D., Toon, G., Risi, C., Scheepmaker, R., Lee, J.-E., Wennberg, P., and Worden, J.: Water vapor isotopologue retrievals from high-resolution GOSAT shortwave infrared spectra, Atmos. Meas. Tech., 6, 263–274, doi:10.5194/amt-6-263-2013, 2013. 9099, 9100

Franz, P. and Röckmann, T.: High-precision isotope measurements of $H_2{}^{16}O$, $H_2{}^{17}O$, $H_2{}^{18}O$, and the $\Delta^{17}O$-anomaly of water vapor in the southern lowermost stratosphere, Atmos. Chem. Phys., 5, 2949–2959, doi:10.5194/acp-5-2949-2005, 2005. 9098

Field, R. D.: Observed and modeled controls on precipitation $\delta^{18}O$ over Europe: from local temperature to the Northern Annular Mode, J. Geophys. Res., 115, D12101, doi:10.1029/2009JD013370, 2010. 9098

Galewsky, J., Strong, M., and Sharp, Z. D.: Measurements of water vapor D/H ratios from Mauna Kea, Hawaii, and implications for subtropical humidity dynamics, Geophys. Res. Lett., 34, L22808, doi:10.1029/2007GL031330, 2007. 9118

AMTD
7, 9095–9135, 2014

Gedzelman, S. D.: Deuterium in water vapor above the atmospheric boundary layer, Tellus B, 40, 134–147, 1988. 9118

Griffith, T, D. W., Jamie, I., Esler, M., Wilson, S. R., Parkes, S. D., Waring, C., and Bryant, G. W.: Real-time measurements of stable isotopes in water and CO_2 by Fourier transform infrared spectrometry, Isot. Environ. Healt. S., 42, 9–20, doi:10.1080/10256010500503098, 2006. 9098

Gupta, P., Noone, D., Galewsky, J., Sweeney, C., and Vaughn, B. H.: Demonstration of high-precision continuous measurements of water vapor isotopologues in laboratory and remote field deployments using wavelength-scanned cavity ring-down spectroscopy (WS-CRDS) technology, Rapid Commun. Mass Spectrom., 23, 2534–2542, doi:10.1002/rcm.4100, 2009. 9098

Herbin, H., Hurtmans, D., Turquety, S., Wespes, C., Barret, B., Hadji-Lazaro, J., Clerbaux, C., and Coheur, P.-F.: Global distributions of water vapour isotopologues retrieved from IMG/ADEOS data, Atmos. Chem. Phys., 7, 3957–3968, doi:10.5194/acp-7-3957-2007, 2007. 9097, 9098

Herbin, H., Hurtmans, D., Clerbaux, C., Clarisse, L., and Coheur, P-F.: $H_2{}^{16}O$ and HDO measurements with IASI/Metop, Atmos. Meas. Phys., 9, 9433–9447, 2009. 9099

Hoffmann, G., Werner, M., and Heimann, M.: Water isotope module of the ECHAM atmospheric general circulation model: a study on timescales from days to several years, J. Geophys. Res., 103, 16871–16896, 1998. 9099, 9103

Jo, K-N., Woo, K. S., Yi, S., Yang, D. Y., Lim, H. S., Wang, Y., Cheng, H., and Edwards, R. L.: Mid-latitude interhemispheric hydrologic seesaw over the past 550,000 yr, Nature, 508, 378–382, doi:10.1038/nature13076, 2014. 9111

Jouzel, J., Alley, R. B., Cuffey, K. M., Dansgaard, W., Grrotes, P., Hoffmann, G., Johnsen, S. J., Koster, R. D., Peel, D., Shuman, C. A., Stievenard, M., Stuiver, M., and White, J.: Validity of the temperature reconstruction from water isotopes in ice cores, J. Geophys. Res., 102, 26471–26487, 1997. 9097

Keith, D. W.: Stratosphere-troposphere exchange: Inferences from the isotopic composition of water vapor, J. Geophys. Res., 105, 15167–15173, 2000. 9118

Kurita, N., Noone, D., Risi, C., Schmidt, G. A., Yamada, H., and Yoneyama, K.: Intraseasonal isotopic variation associated with the Madden-Julian Oscillation, J. Geophys. Res., 116, D24101, doi:10.1029/2010JD015209, 2011. 9111

AMTD
7, 9095–9135, 2014

Lacour, J.-L., Risi, C., Clarisse, L., Bony, S., Hurtmans, D., Clerbaux, C., and Coheur, P.-F.: Mid-tropospheric δD observations from IASI/MetOp at high spatial and temporal resolution, Atmos. Chem. Phys., 12, 10817–10832, doi:10.5194/acp-12-10817-2012, 2012. 9099

Lawrence, J. R., Gedzelman, S. D., Dexheimer, D., Cho, H. K., Carrie, G. D., Gasparini, R., Anderson, C. R., Bowman, K. P., and Biggerstaff, M. I.: Stable isotopic composition of water vapor in the tropics, J. Geophys. Res., 109, D06115, doi:10.1029/2003JD004046, 2004. 9112

Lee, J., Worden, J., Noone, D., Bowman, K., Eldering, A., LeGrande, A., Li, J.-L. F., Schmidt, G., and Sodemann, H.: Relating tropical ocean clouds to moist processes using water vapor isotope measurements, Atmos. Chem. Phys., 11, 741–752, doi:10.5194/acp-11-741-2011, 2011. 9106, 9111

Lee, J.-E. and Fung, I.: "Amount-effect" of water isotopes and quantitative analysis of post-condensation processes, Hydrol. Process., 22, 1–8, doi:10.1002/hyp.6637, 2007. 9111

Lee, X., Sargent, S., Smith, R., and Tanner, B.: In situ measurement of the water vapor $^{18}O/^{16}O$ isotope ratio for atmospheric and ecological applications, Am. Meteorolog. Soc., 22, 555–565, 2005. 9098

Lossow, S., Steinwagner, J., Urban, J., Dupuy, E., Boone, C. D., Kellmann, S., Linden, A., Kiefer, M., Grabowski, U., Glatthor, N., Höpfner, M., Röckmann, T., Murtagh, D. P., Walker, K. A., Bernath, P. F., von Clarmann, T., and Stiller, G. P.: Comparison of HDO measurements from Envisat/MIPAS with observations by Odin/SMR and SCISAT/ACE-FTS, Atmos. Meas. Tech., 4, 1855–1874, doi:10.5194/amt-4-1855-2011, 2011. 9098

Majoube, M.: Oxygen-18 and deuterium fractionation between water and steam, J. Chim. Phys., 68, 1423–1436, 1971a (in French). 9118

Majoube, M.: Fractionation in O-18 between ice and water vapor, J. Chim. Phys., 68, 625–636, 1971b (in French). 9118

Moyer, E. J., Irion, F. W., Yung, Y. L., and Gunson, M. R.: ATMOS stratospheric deuterated water and implications for troposphere–stratosphere transport, Geophys. Res. Lett., 23, 2385–2388, 1996. 9118

Noone, D. and Simmonds, I.: Associations between $\delta^{18}O$ of water and climate parameters in a simulation of atmospheric circulation for 1979–95, J. Clim., 15, 3150–3169, 2002. 9099, 9108

Oort, A. H. and Yienger, J. J.: Observed interannual variability in the Hadley circulation and its connection to ENSO, Am. Meteorolog. Soc., 9, 2751–2767, 1996. 9111

AMTD
7, 9095–9135, 2014

Payne, V. H., Noone, D., Dudhia, A., Piccolo, C., and Grainger, R. G.: Global satellite measurements of HDO and implications for understanding the transport of water vapor into the stratosphere. Q. J. R. Meteorol. Soc. 133, 1459–1471, 2007. 9098

Pommier, M., Lacour, J.-L., Risi, C., Bréon, F. M., Clerbaux, C., Coheur, P.-F., Gribanov, K., Hurtmans, D., Jouzel, J., and Zakharov, V.: Observation of tropospheric δD by IASI over western Siberia: comparison with a general circulation model, Atmos. Meas. Tech., 7, 1581–1595, doi:10.5194/amt-7-1581-2014, 2014. 9106, 9110

Risi, C., Bony, S., and Vimeux, F.: Influence of convective processes on the isotopic composition (δ^{18}O and δD) of precipitation and water vapor in the tropics: 2. Physical interpretation of the amount effect, J. Geophys. Res., 113, D19306, doi:10.1029/2008JD009943, 2008. 9108, 9111

Risi, C., Bony, S., Vimeux, F., and Jouzel, J.: Water-stable isotopes in the LMDZ4 general circulation model: model evaluation for present-day and past climates and application to climatic interpretation of tropical isotopic records, J. Geophys. Res., 115, D12118, doi:10.1029/2009JD013255, 2010. 9099

Risi, C., Noone, D., Worden, J., Frankenberg, C., Stiller, G., Kiefer, M., Funke, B., Walker, K., Bernath, P., Schneider, M., Wunch, D., Sherlock, V., Deuscher, N., Griffith, D., Wennberg, P. O., Strong, K., Smale, D., Mahieu, E., Barthlott, S., Hase, F., García, O., Notholt, J., Warneke, T., Toon, G., Sayres, D., Bony, S., Lee, J., Brown, D., Uemura, R., and Sturm, C.: Process-evaluation of tropospheric humidity simulated by general circulation models using water vapor isotoplogues: 1. Comparison between models and observations, J. Geophys. Res., 117, D05303, doi:10.1029/2011JD016621, 2012a. 9100, 9114, 9115

Risi, C., Noone, D., Worden, J., Frankenberg, C., Stiller, G., Kiefer, M., Funke, B., Walker, K., Bernath, P., Schneider, M., Bony, S., Lee, J., Brown, D., and Sturm, C.: Process-evaluation of tropospheric humidity simulated by general circulation models using water vapor isotopic observations: 2. Using isotopic diagnostics to understand the mid and upper tropospheric moist bias in the tropics and subtropics, J. Geophys. Res., 117, D05304, doi:10.1029/2011JD016623, 2012b. 9110, 9114

Risi, C., Noone, D., Frankenberg, C., and Worden, J.: Role of continental recycling in intraseasonal variations of continental moisture as deduced from model simulations and water vapor isotopic measurements, Water Resour. Res., 49, 4136–4156, doi:10.1002/wrcr.20312, 2013. 9104, 9105, 9106, 9110

AMTD
7, 9095–9135, 2014

Rodgers, C. D. and Connor, B. J.: Intercomparison of remote sounding instruments, J. Geophys. Res., 108, 4116, doi:10.1029/2002JD002299, 2003.
Rozanski, K.: Deuterium and oxygen-18 in European groundwater-links to atmospheric circulation in the past, Chem. Geol., 52, 349–363, 1985. 9111
Scheepmaker, R. A., Frankenberg, C., Galli, A., Butz, A., Schrijver, H., Deutscher, N. M., Wunch, D., Warneke, T., Fally, S., and Aben, I.: Improved water vapour spectroscopy in the 4174–4300 cm^{-1} region and its impact on SCIAMACHY HDO/H_2O measurements, Atmos. Meas. Tech., 6, 879–894, doi:10.5194/amt-6-879-2013, 2013. 9099, 9101, 9109
Schmidt, G. A., Hoffmann, G., Shindell, D. T., and Hu, Y.: Modeling atmospheric stable water isotopes and the potential for constraining cloud processes and stratosphere-troposphere water exchange, J. Geophys. Res., 110, D21314, doi:10.1029/2005JD005790, 2005. 9099
Schmidt, G. A., LeGrande, A. N., and Hoffmann, G.: Water isotope expressions of intrinsic and forced variability in a coupled ocean-atmosphere model, J. Geophys. Res., 112, D10103, doi:10.1029/2006JD007781, 2007. 9099
Schneider, M. and Hase, F.: Optimal estimation of tropospheric H_2O and δD with IASI/METOP, Atmos. Chem. Phys., 11, 11207–11220, doi:10.5194/acp-11-11207-2011, 2011. 9099
Schneider, M., Hase, F., and Blumenstock, T.: Ground-based remote sensing of HDO/H_2O ratio profiles: introduction and validation of an innovative retrieval approach, Atmos. Chem. Phys., 6, 4705–4722, doi:10.5194/acp-6-4705-2006, 2006. 9098
Schneider, M., Yoshimura, K., Hase, F., and Blumenstock, T.: The ground-based FTIR network's potential for investigating the atmospheric water cycle, Atmos. Chem. Phys., 10, 3427–3442, doi:10.5194/acp-10-3427-2010, 2010. 9116, 9118
Schneider, M., Barthlott, S., Hase, F., González, Y., Yoshimura, K., García, O. E., Sepúlveda, E., Gomez-Pelaez, A., Gisi, M., Kohlhepp, R., Dohe, S., Blumenstock, T., Wiegele, A., Christner, E., Strong, K., Weaver, D., Palm, M., Deutscher, N. M., Warneke, T., Notholt, J., Lejeune, B., Demoulin, P., Jones, N., Griffith, D. W. T., Smale, D., and Robinson, J.: Ground-based remote sensing of tropospheric water vapour isotopologues within the project MUSICA, Atmos. Meas. Tech., 5, 3007–3027, doi:10.5194/amt-5-3007-2012, 2012. 9098, 9106, 9110
Smith, R. B.: Deuterium in North Atlantic storm tops, J. Atmos. Sci., 49, 2041–2057, 1992. 9118
Steinwagner, J., Milz, M., von Clarmann, T., Glatthor, N., Grabowski, U., Höpfner, M., Stiller, G. P., and Röckmann, T.: HDO measurements with MIPAS, Atmos. Chem. Phys., 7, 2601–2615, doi:10.5194/acp-7-2601-2007, 2007. 9098

AMTD
7, 9095–9135, 2014

Steinwagner, J., Fueglistaler, S., Stiller, G., von Clarmann, T., Kiefer, M., Borsboom, P. P., van Delden, A., and Röckmann, T.: Tropical dehydration processes constrained by the seasonality of stratospheric deuterated water, Nat. Geosci., 3, 262–266, doi:10.1038/ngeo822, 2010. 9098

Sturm, P. and Knohl, A.: Water vapor δ^2H and δ^{18}O measurements using off-axis integrated cavity output spectroscopy, Atmos. Meas. Tech., 3, 67–77, doi:10.5194/amt-3-67-2010, 2010. 9098

Uemura, R., Matsui, Y., Yoshimura, K., Motoyama, H., and Yoshida, N.: Evidence of deuterium excess in water vapor as an indicator of ocean surface conditions, J. Geophys. Res., 113, D19114, doi:10.1029/2008JD010209, 2008. 9097, 9109, 9111

Uppala, S. M., Kållberg, P. W., Simmons, A. J., Andrae, U., da costa Bechtold, V., Fiorino, M., Gibson, K., Haseler, J., Hernandez, A., Kelly, G. A., Li, X., Onogi, K., Saarinen, S., Sokka, N., Allan, R. P., Andersson, E., Arpe, K., Balmaseda, M. A., Beljaars, A. C. M., van de Berg, L., Bidlot, J., Bormann, N., Caires, S., Chevallier, F., Dethof, A., Dragosavac, M., Fisher, M., Fuentes, M., Hagemann, S., Hólm, E., Hoskins, B. J., Isaksen, L., Janssen, P. A. E. M., Jenne, R., Mcnally, A. P., Mahfouf, J.-F., Morcrette, J.-J., Rayner, N. A., Saunders, R. W., Simon, P., Sterl, A., Trenberth, K. E., Untch, A., Vasiljevic, D., Viterbo, P., and Woollen, J.: The ERA-40 re-analysis, Q. J. R. Meteorol. Soc., 131, 2961–3012, doi:10.1256/qj.04.176, 2005. 9103

Waliser, D. E. and Gautier, C.: A satellite-derived climatology of the ITCZ, J. Climate, 6, 2162–2174, 1993. 9115

Wang, L., Caylor, K. K., and Dragoni, D.: On the calibration of continuous, high-precision δ^{18}O and δ^2H measurements using an off-axis integrated cavity output spectrometer, Rapid Commun. Mass Spectrom., 23, 530–536, doi:10.1002/rcm.3905, 2009. 9098

Webster, R. C. and Heymsfield, J.: Water Isotope Ratios D/H, ^{18}O/^{16}O, ^{17}O/^{16}O in and out of Clouds Map Dehydration Pathways, Sciencemag, 302, 1742–1745, 2003. 9112

Wiegele, A., Schneider, M., Hase, F., Barthlott, S., García, O. E., Sepúlveda, E., González, Y., Blumenstock, T., Raffalski, U., Gisi, M., and Kohlhepp, R.: The MUSICA MetOp/IASI H_2O and δD products: characterisation and long-term comparison to NDACC/FTIR data, Atmos. Meas. Tech. Discuss., 7, 3915–3952, doi:10.5194/amtd-7-3915-2014, 2014. 9099, 9106

Worden, J., Kulawik, S. S., Shephard, M. W., Clough, S. A., Worden, H., Bowman, K., and Goldman, A.: Predicted errors of tropospheric emission spectrometer nadir retrievals from spec-

AMTD
7, 9095–9135, 2014

tral window selection, J. Geophys. Res., 109, D09308, doi:10.1029/2004JD004522, 2004. 9102

Worden, J., Bowman, K., Noone, D., Beer, R., Clough, S., Eldering, A., Fisher, B., Goldman, A., Gunson, M., Herman, R., Kulawik, S. S., Lampel, M., Luo, M., Osterman, G., Rinsland, C., Rodgers, C., Sander, S., Shephard, M., and Worden, H.: Tropospheric emission spectrometer observation of the tropospheric HDO/H_2O ratio: estimation approach and characterization, J. Geophys. Res., 111, D16309, doi:10.1029/2005JD006606, 2006. 9097, 9098, 9100, 9102, 9104, 9105, 9106, 9107, 9108

Worden, J., Noone, D., and Bowman, K.: Importance of rain evaporation and continental convection in the tropical water cycle, Nature, 445, 528–532, doi:10.1038/nature05508, 2007. 9102, 9106, 9111

Worden, J., Noone, D., Galewsky, J., Bailey, A., Bowman, K., Brown, D., Hurley, J., Kulawik, S., Lee, J., and Strong, M.: Estimate of bias in Aura TES HDO/H_2O profiles from comparison of TES and in situ HDO/H_2O measurements at the Mauna Loa observatory, Atmos. Chem. Phys., 11, 4491–4503, doi:10.5194/acp-11-4491-2011, 2011. 9104, 9106

Worden, J., Kulawik, S., Frankenberg, C., Payne, V., Bowman, K., Cady-Peirara, K., Wecht, K., Lee, J.-E., and Noone, D.: Profiles of CH_4, HDO, H_2O, and N_2O with improved lower tropospheric vertical resolution from Aura TES radiances, Atmos. Meas. Tech., 5, 397–411, doi:10.5194/amt-5-397-2012, 2012. 9102, 9105, 9106, 9107, 9108, 9112

Wu, X., Liang, X.-Z., and Zhang, G. J.: Seasonal migration of ITCZ precipitation across the equator: why can't GCMs simulate it?, Geophys. Res. Lett., 30, 1824, doi:10.1029/2003GL017198, 2003. 9115

Wunch, D., Toon, G. C., Wennberg, P. O., Wofsy, S. C., Stephens, B. B., Fischer, M. L., Uchino, O., Abshire, J. B., Bernath, P., Biraud, S. C., Blavier, J.-F. L., Boone, C., Bowman, K. P., Browell, E. V., Campos, T., Connor, B. J., Daube, B. C., Deutscher, N. M., Diao, M., Elkins, J. W., Gerbig, C., Gottlieb, E., Griffith, D. W. T., Hurst, D. F., Jiménez, R., Keppel-Aleks, G., Kort, E. A., Macatangay, R., Machida, T., Matsueda, H., Moore, F., Morino, I., Park, S., Robinson, J., Roehl, C. M., Sawa, Y., Sherlock, V., Sweeney, C., Tanaka, T., and Zondlo, M. A.: Calibration of the Total Carbon Column Observing Network using aircraft profile data, Atmos. Meas. Tech., 3, 1351–1362, doi:10.5194/amt-3-1351-2010, 2010. 9098

Yoshimura, K., Kanamitsu, M., Noone, D., and Oki, T.: Historical isotope simulation using reanalysis atmospheric data, J. Geophys. Res., 113, D19108, doi:10.1029/2008JD010074, 2008. 9099

AMTD
7, 9095–9135, 2014

Yoshimura, K., Frankenberg, C., Lee, J., Kanamitsu, M., Worden, J., and Röckmann, T.: Comparison of an isotopic atmospheric general circulation model with new quasi-global satellite measurements of water vapor isotopologues, J. Geophys. Res., 116, D19118, doi:10.1029/2011JD016035, 2011. 9100, 9104, 9105, 9106, 9111, 9116, 9118

Zakharov, V. I., Imasu, R., Gribanov, K. G., Hoffmann, G., and Jouzel, J.: Latitudinal distribution of the deuterium to hydrogen ratio in the atmosphere water vapor retrieved from IMG/ADEOS data, Geophys. Res. Lett., 31, L12104, doi:10.1029/2004GL019433, 2004. 9098, 9112

Zhang, L., Jacob, D. J., Liu, X., Logan, J. A., Chance, K., Eldering, A., and Bojkov, B. R.: Intercomparison methods for satellite measurements of atmospheric composition: application to tropospheric ozone from TES and OMI, Atmos, Chem, Phys., 10, 4725–4739, doi:10.5194/acp-10-4725-2010, 2010. 9108

AMTD
7, 9095–9135, 2014

Table 1. Comparison of satellite instruments and model used in this study.

Comparison	TES	SCIAMACHY	ECHAM
Wavelength	650–3050 cm^{-1}	2355–2375 nm	–
Mode	Limb, Nadir	Limb, Nadir, Sun/Moon Occultations	–
Sensitivity	500–850 hPa (v4) and 425–900 hPa (v5)	total column	–
Resolution	5.3 km × 8.4 km	120 km × 30 km	2.8° × 2.8°
Layers used	28 (v4) and 17 (v5)	–	6 layers interpolated to TES layers
Data used	2006	2003–2005	2001

AMTD
7, 9095–9135, 2014

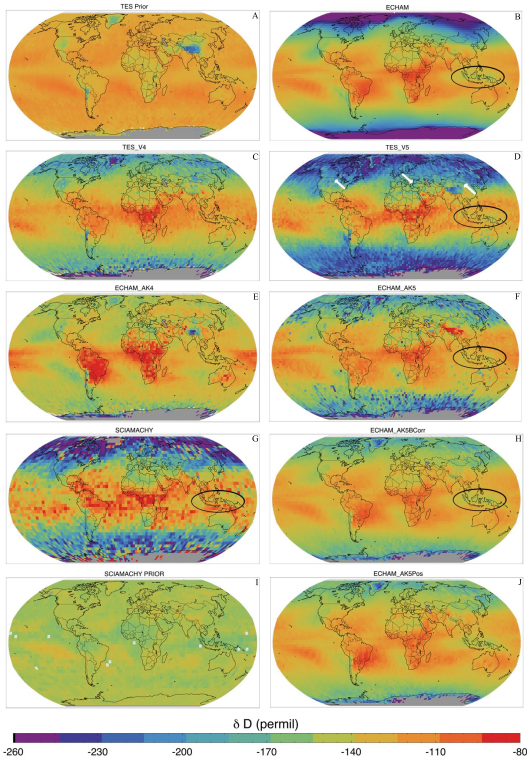

Figure 1. TES prior version 4 **(A)**, ECHAM model input **(B)**, δD product from TES_{V4} **(C)**, TES_{V5} **(D)**, $ECHAM_{AK4}$ **(E)**, $ECHAM_{AK5}$ **(F)**, SCIAMACHY **(G)** and $ECHAM_{AK5Corr}$ **(H)**, SCIAMACHY prior **(I)**, and $ECHAM_{AK5Pos}$ plot **(J)**. The figures of TES prior, TES_{V4}, and $ECHAM_{AK4}$ are averaged between 850–500 hPa and TES_{V5}, $ECHAM_{AK5}$, $ECHAM_{AK5Corr}$, and $ECHAM_{AK5Pos}$ between 900–425 hPa. The results are bias corrected by 5 %, 3 %, and −5 ‰ for TES_{V4}, $ECHAM_{AK4}$, and SCIAMACHY, respectively. Arrows in **(D)** point out the continental effect and ellipses in **(B)**, **(D)**, **(F)**, **(G)**, **(H)** show the region with a strong isotope amount effect around Indonesia. All plots are annual average δD.

AMTD
7, 9095–9135, 2014

Global scale remote sensing of water isotopologues

S. J. Sutanto et al.

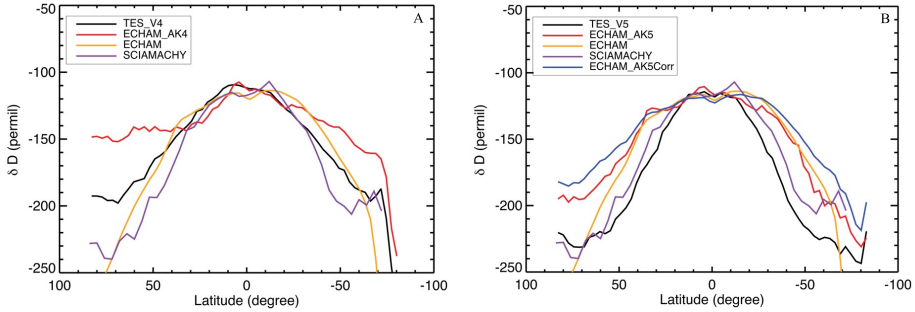

Figure 2. Annual average latitude profile of δD in water vapor from TES, ECHAM, $ECHAM_{AK}$, $ECHAM_{AK5Corr}$, and SCIAMACHY. In **(A)** the TES for version 4 datasets are shown and in **(B)** the TES version 5 datasets.

AMTD
7, 9095–9135, 2014

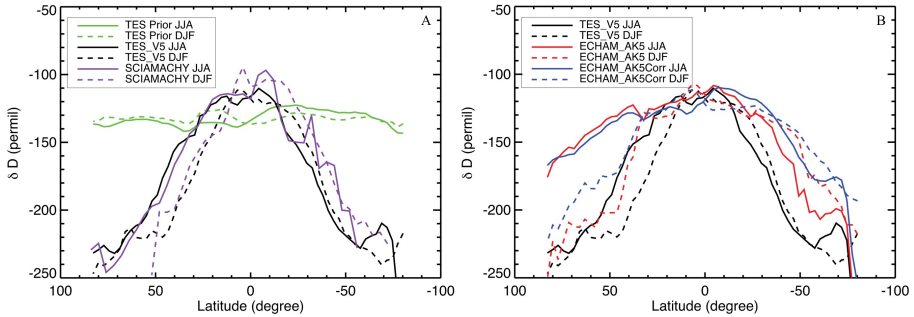

Figure 3. Seasonal comparison of zonal means of δD from TES prior, TES_{V5} and SCIAMACHY **(A)**, and from TES_{V5}, $ECHAM_{AK5}$, and $ECHAM_{AK5Corr}$ **(B)**. Solid lines show NH summer profiles and dashed lines NH winter profiles.

AMTD
7, 9095–9135, 2014

Global scale remote sensing of water isotopologues

S. J. Sutanto et al.

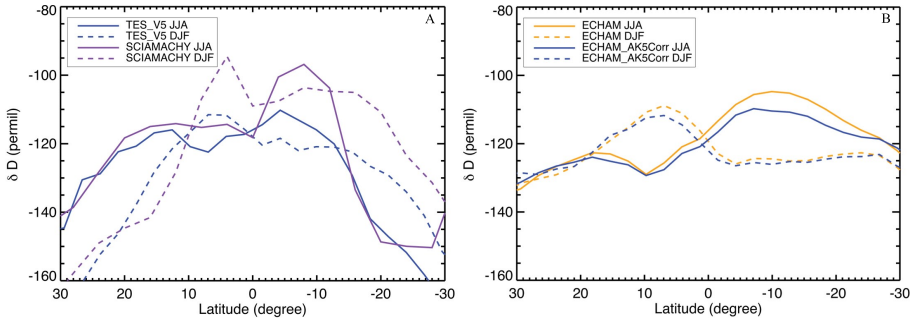

Figure 4. Latitudinal δD profiles between 30° N and 30° S in northern summer (JJA, solid lines) and northern winter (DJF, dashed lines) of TES_{V5} and SCIAMACHY **(A)**; ECHAM and $ECHAM_{AK5Corr}$ **(B)**.

AMTD
7, 9095–9135, 2014

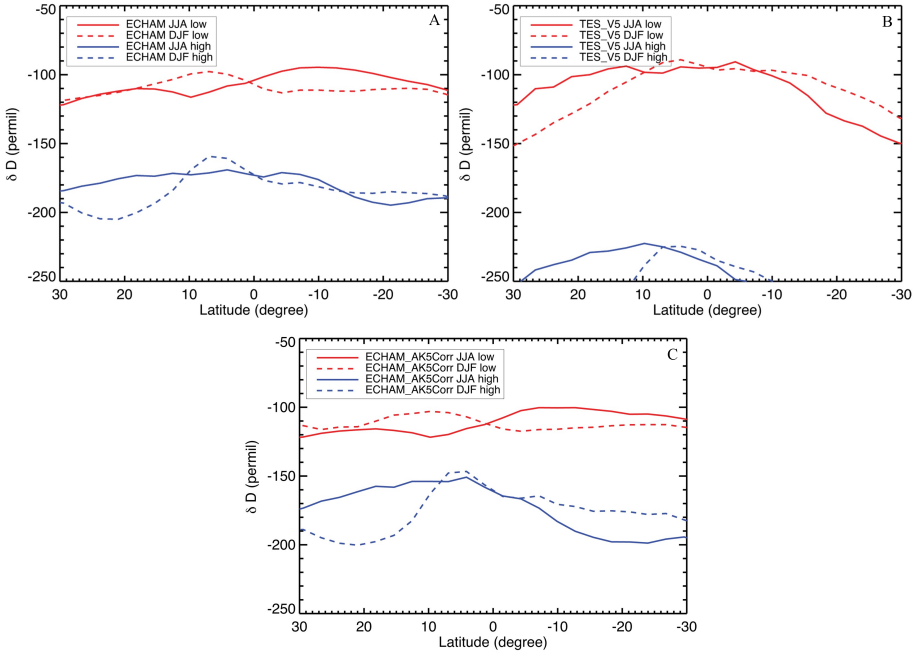

Figure 5. Latitudinal profiles between 30° N and 30° S in northern summer (JJA, solid lines) and northern winter (DJF, dashed lines) of ECHAM from 900 to 680 hPa and from 618 to 425 hPa **(A)**, of TES_{V5} from 900 to 680 hPa and from 618 to 425 hPa **(B)**, and of $ECHAM_{AK5Corr}$ from 900 to 680 hPa and from 618 to 425 hPa **(C)**.

AMTD
7, 9095–9135, 2014

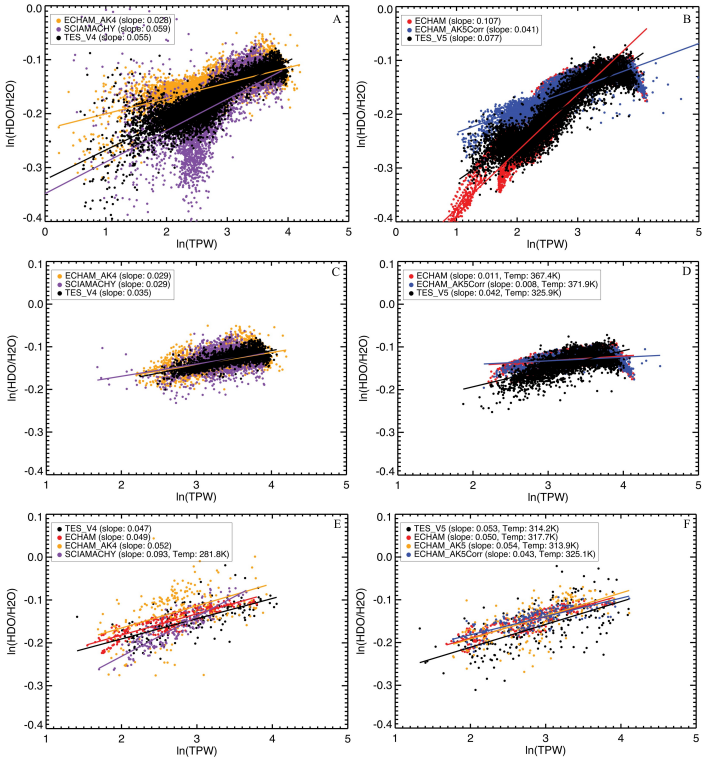

Figure 6. Correlation plot of ln (TPW) (Total Precipitable Water derived from specific humidity) vs. model simulated and satellite retrieved ln(HDO/H_2O). **(A)** and **(B)** global correlations. **(C)** and **(D)** Correlations in the tropics (30° N–30° S). **(E)** and **(F)** Correlations in the Sahel region. Panels **(A)**, **(C)**, and **(E)** show the version 4 TES datasets and SCIAMACHY. Panels **(B)**, **(D)**, **(F)** show the version 5 TES datasets, both together with $ECHAM_{AK}$. ECHAM plot at the left side is averaged from 850–500 hPa and ECHAM plot at the right side is averaged from 900–425 hPa.

AMTD
7, 9095–9135, 2014